Master of Science Thesis
HT2021

Quantification of Fatty Acid Composition in Short T2* Tissue Using MRI – Comparison of 3 T and 7 T

Felix Månsson

Supervisors

Pernilla Peterson, Lund

This work has been conducted at
the Medical Radiation Physics,Malmö and at SUS, Malmö

Medical Radiation Physics, Lund
Faculty of Science
Lund University
www.msf.lu.se

Abstract

Purpose: To optimize a method and develop an algorithm to quantify Fatty Acid Composition (FAC) in bone marrow adipose tissue. By using different reconstruction models, compare different MRI systems (3 T and 7 T) to find the optimal field strength and reconstruction model for FAC quantification. Also, to develop a reference phantom with bone marrow-like characteristics.

Method: Multi-echo GRE (Gradient Echo) data was acquired from a 3 T Siemens and a 7 T Philips system using phantoms made from different commercial butters. Proton density fat fraction (PDFF), Saturated fatty acids (SFA) and poly-unsaturated fatty acids (PUFA) were estimated using three different reconstruction models: constrained, free and original. Quantification agreement and method robustness was compared between systems and models using linear regression, Bland-Altman analysis, and relative errors.

Results: When comparing the MRI-measurements with the theoretical values from the commercial butters, overall, PDFF is the most robust variable with high quantification agreement. In general, SFA was underestimated across all models for both field strengths, while PUFA in general was slightly overestimated. For both SFA and PUFA, comparing 3 T and 7 T, the 3 T system shows more robustness to errors and changes in the method than the 7 T system. Model-wise, the constrained model showed both more robust results and higher agreement than the free and original models. The algorithm that has been developed works for reconstruction of FAC images for 3 T Philips and 7 T Siemens MRI systems. The constructed reference phantoms may be used to estimate FAC at low T2* and different FAC, however, cannot be used to estimate FAC at different T2*.

Conclusion: Commercial butters has proven to be a reasonable reference phantom to simulate tissue with short T2*. For future studies of FAC in bone marrow adipose tissue, 3 T with a constrained approach is preferred over 7 T.

Keywords: MRI, fatty acid composition, bone marrow adipose tissue, fat quantification, field strength comparison

Populärvetenskaplig sammanfattning

Syftet med denna studie är att jämföra olika metoder att kvantifiera den kemiska fettsammansättningen i benmärg med hjälp av magnetkamerateknik, att jämföra dessa metoder för två olika magnetfältsstyrkor samt att ta fram referensfantom och beräkningsalgoritmer för att uppskatta fettinnehållet.

Magnetresonans, eller MR, är en vanlig diagnostisk teknik inom vården. Magnetkameran använder sig av ett starkt magnetfält för att få en signal från kroppens vatten och fett, och på så sätt skapa en bild. Detta gör att tekniken är ett bra val för att göra undersökningar av kroppens mjukdelar, som till exempel benmärg, utan att behöva göra ett kirurgiskt ingrepp. Hur stark signal som fås, och vilken bildupplösning man kan uppnå, beror bland annat på styrkan på magnetkamerans magnetfält. På ett typiskt sjukhus finns magnetkameror med styrkorna 1,5 T och 3 T, men i Lund finns även Sveriges enda magnetkamera med styrkan 7 T.

Artros är en folksjukdom som drabbar kroppens leder och orsakar smärta och stelhet till exempel genom att brosk bryts ner och försvinner. I dagsläget finns ingen behandling som kan bota eller bromsa artros, och sjukdomen upptäcks först när brosket i leden redan är borta. För patienten återstår då endast smärtlindring eller att byta ut leden. Att hitta en metod för tidig diagnos av artros är därför av stor vikt för att i framtiden kunna utveckla sätt att hindra, eller sakta ner, nedbrytningen av brosk innan det är för sent. Artros drabbar dock inte bara brosket utan också andra vävnader i hela leden. Vi behöver därför även förstå hur dessa andra vävnader, så som benmärg, påverkas av artros.

Benmärgen finns i skelettet och en stor mängd av denna benmärg består av fett. Beroende på sammansättningen kan detta fett beskrivas som mättat fett, enkelomättat fett, eller fleromättat fett. Mängden mättat fett ökar med ålder, samt ökar vid vissa sjukdomar. Fler studier krävs för att avgöra om mängden mättat fett även förändras vid artros. För dessa studier behövs verktyg som låter oss mäta benmärgens fettsammansättning.

Med hjälp av avancerade beräkningar kan vi ta fram en metod för att beräkna halterna mättat, enkelomättat och fleromättat fett i benmärgen från insamlade MR-bilder. För att optimera metoden inför kliniska studier används i detta arbete mätningar i provrör med kända innehåll. På detta sätt har vi ett facit på fettinnehållet, och kan på så sätt jämföra vilken teknik och magnetfältsstyrka som bäst kan uppskatta fettsammansättning i benmärg.

Resultaten påvisar att ett MR-system med en magnetfältsstyrka på 3 T ger stabilare resultat vid mätningar av mättat och fleromättat fett än MR system på 7 T, samt att metoden som tagits fram kan uppskatta mättat och omättat fett till en duglig grad.

Abbreviations
OA = Osteoarthritis
FA = Fatty Acid
FAC = Fatty Acid Composition
MRI = Magnetic Resonance Imaging
MRS = Magnetic Resonance Spectroscopy
SFA = Saturated Fatty Acid
MUFA = Mono-Unsaturated Fatty Acid
PUFA = Poly-Unsaturated Fatty Acid
PDFF = Proton Density Fat Fraction
ndb = Number of Double Bonds
nmidb = Number of Methylene-Interrupted Double Bonds
cl = Chain Length
SNR = Signal-to-Noise Ratio
TE = Echo Time
ΔTE = Time Between Echoes
GRE = Gradient Echo
GC = Gas Chromatography

Symbols
$S(t)$ = Signal
W = Water Fraction
F = Fat Fraction
α_m = Amplitudes of Fat Peaks
Δf_m = Difference in Frequency between fat peak m and water
t = Echo Time
T_2^* = Transversal Relaxation
ψ = Off-Resonance Frequency
$\hat{\psi}$ = Complex Field-Map
θ_{bip} = Bipolar Phase Error
$Bi_{bip} = [-1,1,-1,1,-1,1,-1,1]$
θ_{int} = Interleaved Phase Error
$Bi_{int} = [-1,-1,1,1,-1,-1,1,1]$

Table of Contents

Introduction 5
Osteoarthritis 5
Bone Marrow 5
MRI-Based FAC Quantification atty Acid Composition 6
3T vs 7T 6
Aims 7
Theory 7
Imaging Sequence 7
Signal Equation 8
Basic Signal Equation 8
Calculation Step 1 – Iterative Estimation of Complex Field and Phase Error Maps 9
Calculation Step 2 – Estimation of FAC Parameters 10
Different Fat Models 11
Constrained 11
Free 11
Original 12
Method 13
Phantoms 13
Imaging 15
ROI Selection 16
Image Analysis 16
Results 17
Early Phantom Trials 17
Final Phantom Trials 19
Comparisons 20
PDFF 20
SFA 23
PUFA 26
Discussion 28
Conclusion 30
Acknowledgements 30
References 30

Introduction

The importance of being able to quantify the fat content has with the years steadily increased and methods for fat quantification using Magnetic Resonance Imaging (MRI) have been widely used. There are established methods for quantifying fat fractions, however, there have also been methods emerging to estimate the fatty acid composition (FAC) in adipose tissue using both MRI and Magnetic Resonance Spectroscopy (MRS) (1, 2). Methods for quantifying and calculating FAC have recently started being developed and used also for fats in bone marrow adipose tissue (3, 4). It has been suggested that diseases such as osteoarthritis may give rise to changes in the amount of fatty acids in bone marrow (5, 6).

Osteoarthritis

Osteoarthritis (OA) is a chronic degenerative disorder which often causes pain in the joints affected. The pain usually increases when weight is put on the joints or with activity. The condition is characterized by degeneration of cartilage, as well as bone remodeling near joints. Most often OA is related to aging (7), but the cause of OA is not completely known (8).

Every fourth person above 45 years of age in Sweden has some type of arthritis, and the prevalence is increasing. OA of the knee is the most common form of OA and doubles the risk of sick leave. (9)

Even though OA is very common and has a large negative impact, options for treating OA are currently very limited, and treatment for stopping or changing its progression is currently not available (10, 11).

The increase in OA makes it more important than ever to find a way to identify the disease in its early stages, before the cartilage has started deteriorating to the point where debilitating symptoms appear. It also gives importance to finding out more about how other tissue in the joint, such as bone marrow, is affected by the disease.

Bone Marrow

The bone marrow consists of hematopoietic tissue (where red blood cells are made) and adipose tissue (fat). These two types of tissue are both contained within a network of cancellous bone. Bone marrow exists in axial and long bones throughout the body. (12)

The largest change in bone marrow with age is a conversion of red bone marrow to yellow bone marrow (13). That is, less and less of the bodies bone structure produce red blood cells with age. At age 18, the whole skeleton is haematopoietically active, producing red blood cells. By age 65, only around 30% of the bone is active (13, 14). This is followed by an equivalent increase in bone marrow fat. The increase in fat in the bone marrow has been correlated to an increase in incidence and severity of osteoporosis (15). In adults, bone marrow contains approximately 60-90% fat, depending on age and disease (3).

So far, studies have found that patients with OA have a larger concentration of fatty acids, both in the cartilage and in the bone marrow of the femoral head (5, 6). Osteoarthritic bone was found to have the double mass amount of fat per volume of

bone tissue (6). But not only is there a change in the concentration of fatty acids, but also FAC seems to be affected. Changes in the amount of unsaturated and saturated lipids has been seen in and around the bone marrow of the knee joint (16-19). This makes it important to not only look at the fat content of the bone marrow, but also the FAC.

The challenge with using MR for fat quantification for bone marrow adipose tissue compared to, for example, subcutaneous fat is that the fat in bone marrow has a shorter T2* relaxation. In addition, the fat content may be lower in bone marrow. (20)

MRI-Based FAC Quantification

The most common type of lipid in the human body is made up of triglycerides. Triglycerides are made from a glycerol backbone with three fatty acid chains connected to it. Each of these fatty acid chains contain different amounts of carbon atoms, and double bonds between them. (21) Depending on the amount of double bonds, the FAC may be described as saturated (SFA, containing no double bonds), unsaturated (UFA, containing at least one double bond), monounsaturated (MUFA, containing one double bond) or polyunsaturated (PUFA, containing at least two double bonds).

Both MRI and MRS offer a non-invasive method to look at fat composition. However, MRI can offer a higher spatial resolution image over a much larger volume than MRS can. FAC quantification has been compared to gas chromatography for both MRS and MRI. In that comparison, MRI proved to have a stronger correlation to GC than MRS did. (22)

The method used in this study utilizes the differences in signal frequency between different fat peaks, and water, to separate them from each other (2). These fat peaks correspond to different parts of the fat molecule (1). Using this, and the number of double bonds, the FAC can be estimated (2).

3T vs 7T

In general, the signal increases with increasing field strength due to increased magnetization. This also implies an increase to the Signal-to-Noise-Ratio (SNR) which e.g, may be utilized to obtain a higher spatial detail. However, T2* decreases when increasing the field strength (23). This decrease in T2* can potentially make it harder to collect signal during a long enough period to be able to separate different fat peaks. As the B0 field homogeneity increases with increasing field strength (24), it also becomes more important in being able to correct for these inhomogeneities.

Not only does T2* decrease with increasing field strength, but the speed at which the phase between water and different fat peaks evolves also increases. This in turn means that a smaller ΔTE (time between echoes) is needed to be able to estimate FAC. (25)

As stated in the sections above, the technique of quantifying FAC has been validated when measuring in subcutaneous fat, however, it is more challenging using the technique to measure fat in bone marrow, because of a very short T2* relaxation

time. Because of this difference, a reconstruction model for fat needs to be decided upon and a field strength needs to be chosen to find the optimal method of quantifying fatty acids in short T2* tissue.

Aims

- To optimize a method and develop a reconstruction algorithm for quantifying FAC in bone marrow adipose tissue using MRI for use in studies of OA.
    - Develop an algorithm for FAC reconstruction in Python
    - Develop a reference phantom with bone marrow-like characteristics
    - Compare 3T and 7T
    - Compare reconstruction models

Theory

In this section, the theory behind the imaging sequence, signal equations, calculations, and fat models will be described. Also, the different phase error corrections, and conversions to FAC will be shown.

The calculations were done using two calculation steps. The first step was a pure separation of the fat and water, estimation of the complex field-map and phase errors. The complex field-map and phase errors are then used in the second calculation step, where a separation of FAC is done, that is, separation of the number of double bonds (ndb), number of methylene-interrupted double bonds (nmidb) and the chain length (cl). The bonds are then converted into fractions of SFA and PUFA. PDFF (Proton Density Fat Fraction) is calculated from the estimated water (W, step 1) and fat (F, step 2) signals, according to PDFF = F/(W+F). T2* is extracted from the complex field-map in calculation step one. Expected average T2* values in tibial bone marrow range from 30-70 ms (20), depending on field strength and voxel size.

Imaging Sequence

The imaging sequence used was a multi-echo GRE (Gradient Echo) bipolar interleaved sequence. The aim is to sample the signal evolution over time with several tightly spaced echoes.

Using a bipolar readout means that the readout gradient is done in both directions, and an interleaved acquisition means that two different GRE sequences are used. The echoes of the second sequence are displaced ΔTE/2 compared to the first sequence. The images from the two sequences are then combined to a single data set with an effective ΔTE=ΔTE/2. Figure 1 shows a basic bipolar interleaved multi-echo GRE sequence.

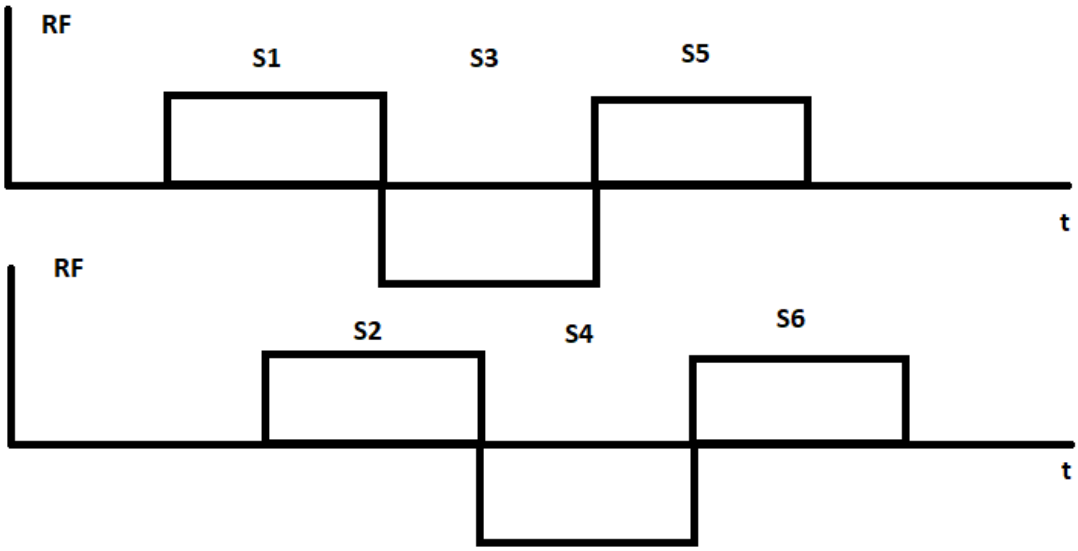

Figure 1: Read-out gradients of a Bipolar Interleaved GRE sequence. RF represents the Radio Frequency pulse, and S# represents collected echoes.

A sequence like this, however, introduces phase errors that needs to be corrected for. One phase error occurs because of the bipolarity of the readout within one sequence. The phase error from the bipolar readout is an issue because of the phase polarity change between the sequences, unlike a unipolar sequence which has the same polarity of the phase error. (26, 27)

By using an interleaved scan, more echoes can be collected with shorter time in between the echoes. This, however, adds yet another phase error that needs to be corrected for, since the phase between the two sequences can differ. (27)

Signal Equation

Basic Signal Equation

The model used to describe the signal evolution with echo time, t, from a voxel containing water and fat is:

$$S(t) = \left[W + F\sum_{m}^{M} \alpha_m e^{i2\pi\Delta f_m t}\right] e^{-\frac{t}{T_2^*}} * e^{i2\pi\psi t} * e^{i\theta_{bip}Bi_{bip}} * e^{i\theta_{int}Bi_{int}} \qquad (1)$$

Where Δf_m is the difference in frequency between fat peak m, and the water peak, and M is the number of fat peaks in the model. T_2^* is the transversal relaxation time and ψ is the off-resonance frequency. α_m represents the amplitude of the fat peak m. The last two exponentials represent the bipolar and interleaved phase error corrections where θ_{bip} and θ_{int} are the respective phase errors, $Bi_{bip} = [-1,1,-1,1,-1,1,-1,1]$ and $Bi_{int} = [-1,-1,1,1,-1,-1,1,1]$.

Equation *(1)* is transformed into matrix form to simplify the calculations. For simplicity, this is done by firstly creating a complex field-map $\psi = \psi + \frac{i}{2\pi T_2^*}$, then $e^{-\frac{t}{T_2^*}}$

and $e^{i2\pi\psi t}$ can be combined into $e^{i2\pi\psi t}$. A complex field identity matrix $\boldsymbol{D_{NxN}}$, is then made using this combination and the phase error corrections.

$$D_{NxN} = \begin{bmatrix} e^{i2\pi\psi t_1} * e^{i\theta_{bip}Bi_{bip}} * e^{i\theta_{int}Bi_{int}} & \cdots & 0 \\ \vdots & \ddots & \vdots \\ 0 & \cdots & e^{i2\pi\psi t_N} * e^{i\theta_{bip}Bi_{bip}} * e^{i\theta_{int}Bi_{int}} \end{bmatrix} \quad (2)$$

Where N is the number of echoes. Further, a Nx2 frequency matrix **A** needs to be defined:

$$A_{Nx2} = \begin{bmatrix} 1 & \sum_m^M \alpha_m e^{i2\pi\Delta f_m t_1} \\ . & . \\ . & . \\ 1 & \sum_m^M \alpha_m e^{i2\pi\Delta f_m t_N} \end{bmatrix} \quad (3)$$

Here, the left column represents the water, and the right column represents the frequency components of the fat for each echo time.

The amplitudes of the different peaks can be represented as a 2x1 matrix, $\boldsymbol{\rho}$.

$$\rho_{2x1} = \begin{bmatrix} W \\ F \end{bmatrix} \quad (4)$$

Where W is the fraction of water, F is the fraction of fat.

By using the amplitudes and frequency components from **A**, the complex field identity matrix, and fractions from $\boldsymbol{\rho}$, the signal **S**, can be calculated as seen in equation *(1)*, as several matrices instead:

$$S = D * A * \rho \quad (5)$$

If the complex field map and the phase errors are known, an estimation of $\boldsymbol{\rho}$ can be done using:

$$\rho = (D * A) \backslash S \quad (6)$$

Calculation Step 1 – Iterative Estimation of Complex Field and Phase Error Maps

If a reconstruction model is now considered instead of a general model, another Nx5 matrix, **B**, can be created. The goal here is to find the complex field map and the phase error maps, so that $\boldsymbol{\rho}$ from equation *(6)* can be calculated.

$$B_{Nx5} = \begin{bmatrix} 1 & \sum_m^M \alpha_m e^{i2\pi\Delta f_m t_1} & i2\pi t_1 (W + F\sum_m^M \alpha_m e^{i2\pi\Delta f_m t_1}) & iBi_{bip}(W + F\sum_m^M \alpha_m e^{i2\pi\Delta f_m t_1}) & iBi_{int}(W + F\sum_m^M \alpha_m e^{i2\pi\Delta f_m t_1}) \\ \vdots & \vdots & \vdots & \vdots & \vdots \\ 1 & \sum_m^M \alpha_m e^{i2\pi\Delta f_m t_N} & i2\pi t_N (W + F\sum_m^M \alpha_m e^{i2\pi\Delta f_m t_N}) & iBi_{bip}(W + F\sum_m^M \alpha_m e^{i2\pi\Delta f_m t_N}) & iBi_{int}(W + F\sum_m^M \alpha_m e^{i2\pi\Delta f_m t_N}) \end{bmatrix} \quad (7)$$

This matrix is dependent on water, each frequency component of the fat, the complex field map, and the phase errors of the bipolar and interleaved sequence. A relation between **S**, **B** and another 5x1 matrix can then be found:

$$\begin{bmatrix} W \\ F \\ \Delta\hat{\psi} \\ \theta_{bip} \\ \theta_{int} \end{bmatrix} = B \backslash S \quad (8)$$

An iterative method is used to determine $\hat{\psi}$ and the phase errors. A first guess of $\hat{\psi}$ and the phase errors are made. This means that a first guess of the $\boldsymbol{\rho}$ and **D** matrices can be made using equation *(6)* and *(2),* respectively. A new $\hat{\psi}$ and new phase errors can then be calculated through equation *(8)*, and the value of $\Delta\hat{\psi}$, θ_{bip} and θ_{int} are added onto the first guess of the respective parameter**.** The process is then repeated, until a small enough difference between iterations is achieved.

Calculation Step 2 – Estimation of FAC Parameters

Now that the complex-field map is determined, the FAC parameters can be calculated, also iteratively. This is done by calculating $\boldsymbol{\rho}$ through equation (6), using the now found complex field and phase error maps. The calculation is made using three different reconstruction models. Each model will have different $\boldsymbol{\rho}$ and **A** matrices depending on the number of parameters calculated.

The fat models and signal model are based upon the suggestion from Hamilton et al (1), which describes the fat spectrum using ndb, nmidb and cl. This means that the amplitude of each fat peak (α_m) can be described using these three parameters and are calculated similarly to parameters W and F in the basic signal model.

As suggested by Peterson et al. (2), ndb, nmidb and cl can be converted into FA fractions. Percentages of SFA, PUFA and MUFA are calculated from ndb, nmidb and cl according to equation (*9-12)*.

$$UFA = \frac{(ndb - nmidb)}{3} * 100 \quad (9)$$

$$PUFA = \frac{nmidb}{3} * 100 \quad (10)$$

$$MUFA = UFA - PUFA \tag{11}$$

$$SFA = 100 - UFA \tag{12}$$

Different Fat Models

Three different fat models were evaluated: constrained, free, and original. The number of variables calculated in the fat estimation varies depending on the model. Here, for convenience, $e^{i2\pi\Delta f_m t}$ is denoted as E_m (22).

Constrained

The constrained model only estimates ndb. Nmidb and cl are then calculated using empirical linear relationships based on GC analysis of subcutaneous adipose tissue (22). This means that the constrained model needs fewer datapoints, since it calculates fewer variables. Nmidb is calculated from ndb by $nmidb = 0.45 * \mathrm{ndb} - 0.71$, and cl is calculated with $cl = 16.32 + 0.38 * ndb$.

The constrained model **A** matrix looks like the following:

$$A_{Nx3} = \begin{bmatrix} 1 & a(t_m) & b(t_m) \\ . & . & . \\ . & . & . \\ 1 & a(t_M) & b(t_M) \end{bmatrix} \tag{13}$$

When each peak is expressed in terms of ndb, nmidb and cl, they can be described as the following (2, 22):

$$a(t) = E_1(t) + 4E_2(t) - 1.42E_3(t) + 6E_4(t) + 2.84E_5(t) + 6E_6(t) + 72.5E_7(t) + 9E_8(t) \tag{14}$$

$$b(t) = 2E_1(t) + 0.9E_3(t) + 2.2E_5(t) - 4.82E_7(t) \tag{15}$$

The constrained model $\boldsymbol{\rho}$ matrix looks like the following:

$$\rho_{3x1} = \begin{bmatrix} W \\ F * k \\ F * k * ndb \end{bmatrix} \tag{16}$$

Where k is the sum of all fat peak amplitudes.

Free

The free model estimates ndb and nmidb. Cl is then calculated the same way from ndb as in the constrained model. The free model **A** matrix looks like the following:

$$A_{Nx4} = \begin{bmatrix} 1 & a(t_m) & b(t_m) & c(t_m) \\ . & . & . & . \\ . & . & . & . \\ 1 & a(t_M) & b(t_M) & c(t_M) \end{bmatrix} \quad (17)$$

When each peak is expressed in terms of ndb, nmidb and cl, they can be described as the following (2, 22):

$$a(t) = E_1(t) + 4E_2(t) + 6E_4(t) + 6E_6(t) + 73.92E_7(t) + 9E_8(t) \quad (18)$$

$$b(t) = 2E_1(t) + 4E_5(t) - 5.72E_7(t) \quad (19)$$

$$c(t) = 2E_3(t) - 4E_5(t) + 2E_7(t) \quad (20)$$

The free model $\boldsymbol{\rho}$ matrix looks like the following:

$$\rho_{4x1} = \begin{bmatrix} W \\ F * k \\ F * k * ndb \\ F * k * nmidb \end{bmatrix} \quad (21)$$

Original

The original model estimates all three variables, this means that there is no assumed linear connection between them. Because of this the original model needs more data points than previous models since there are more unknowns. The original model **A** matrix looks like the following:

$$A_{Nx5} = \begin{bmatrix} 1 & a(t_m) & b(t_m) & c(t_m) & d(t_m) \\ . & . & . & . & . \\ . & . & . & . & . \\ 1 & a(t_M) & b(t_M) & c(t_M) & d(t_M) \end{bmatrix} \quad (22)$$

When each peak is expressed in terms of ndb, nmidb and cl, they can be described as the following (2, 22):

$$a(t) = E_1(t) + 4E_2(t) + 6E_4(t) + E_6(t) - 24E_7(t) + 9E_8(t) \quad (23)$$

$$b(t) = 2E_1(t) + 4E_5(t) + 8E_7(t) \quad (24)$$

$$c(t) = 2E_3(t) - 4E_5(t) + 2E_7(t) \quad (25)$$

$$d(t) = 6E_7(t) \tag{26}$$

The original model $\boldsymbol{\rho}$ matrix looks like the following:

$$\rho_{5x1} = \begin{bmatrix} W \\ F * k \\ F * k * ndb \\ F * k * nmidb \\ F * k * cl \end{bmatrix} \tag{27}$$

Method

Phantoms

The goal when creating the phantoms was to try and create a bone marrow adipose tissue-like phantom setup and to have a range of FAC. In addition, we wanted to be able to construct phantoms with different fat fractions and T2*, but identical FAC in order to observe how the FAC estimations are impacted by T2* and fat content.
To achieve this, different types of phantoms were tested: Commercial butters (short T2*) and vegetable oils (long T2*). By using commercial fats and oils, a priori knowledge of the content of the butter and oils was available as reference values from the butter packages.

To vary the T2* for the different butters and oils, different methods were tested. By changing the temperature, theoretically, the T2* of both the butters and oils would be affected. Also, by introducing a sponge into the oil to try and simulate cancellous bone, an attempt at altering T2* was made.

To control the PDFF of the butters, a set of clarified butters with PDFF = 100 % was constructed. This was done because no commercial butter with 100% PDFF was available. For lower ranges of PDFF, different commercial butters were available.

Table 1: Phantom layout and fat fractions of the different phantoms. 1a-6a defines the 100% fat fraction butters, 1b-6b defines the 80% fat fraction butters and 1c-4c defines the PDFF series ranging from 40% fat fraction to 100% fat fraction.

Butter	Phantom Number	Fat Fraction%	SFA%	MUFA%	PUFA%
Flora Växtbaserad (Clarified)	1a	100	23	54	23
ICA Mat & Bak Margarin (Clarified)	2a	100	34	49	16
Milda Mat och Bak (Clarified)	3a	100	39	46	16
Carlshamn Mjölkfritt (Clarified)	4a	100	44	41	15
ICA Mjölkfritt Margarin (Clarified)	5a	100	47	38	14
Arla, Svenskt Smör (Clarified)	6a	100	70	27	3
Flora Växtbaserad	1b	79	23	54	23
ICA Mat & Bak Margarin	2b	80	34	49	16
Milda Mat och Bak	3b	80	39	46	16
Carlshamn Mjölkfritt	4b	80	44	41	15
ICA Mjölkfritt Margarin	5b	79	47	38	14
Arla, Svenskt Smör	6b	80	70	27	3
Bregott Mindre	1c	38	41	44	16
Flora Mjölkfritt	2c	59	41	44	15
Milda Mat och Bak	3c	80	39	46	15
Milda Mat och Bak (Clarified)	4c	100	39	46	15

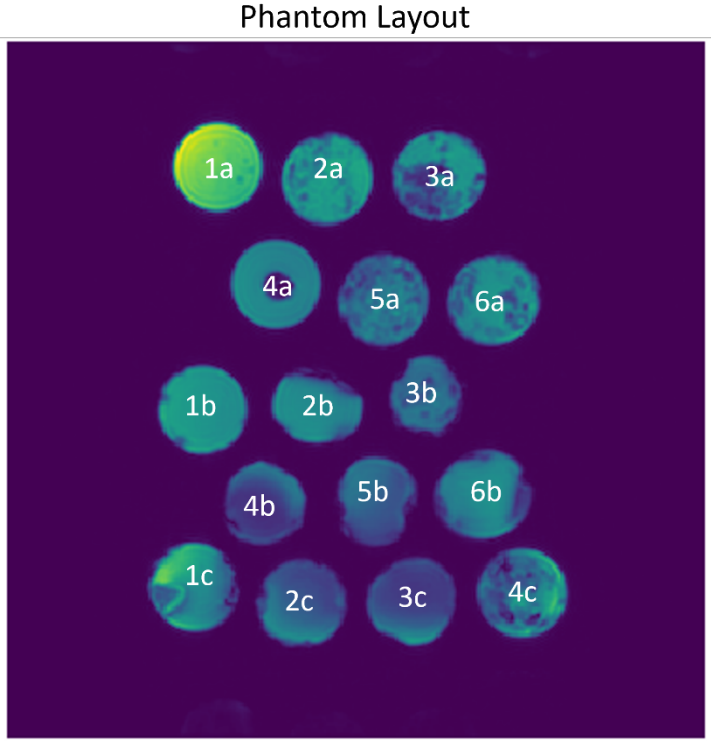

Figure 2: Setup of the final three sets of phantoms setup. Phantoms 1a-6a are 100% fat, phantoms 1b-6b are 80% fat, phantoms 1c-4c is a pdff series consisting of 40, 60, 80 and 100% fat, respectively.

Finally, three sets of phantoms with a range of FAC values were chosen for continued experiments to compare methods and field strengths: one of 80% fat, one of 100% fat, and a PDFF series. This setup can be seen in figure 2 and table 1. All three sets were measured at room temperature. The two FAC setups have the same butters, with the only difference that the 100% phantom set is clarified. Sadly, a phantom setup with long T2* was not included in the final phantom setup due to construction difficulties.

Imaging

The final phantom setup was imaged using a Siemens Prisma 3 T and a Philips Achieva 7 T. The sequence used is a 3D GRE sequence.

The scan protocols for the 3 T and 7 T measurements were made as similar to each other as possible. Scan protocols can be seen in table 2. The TEs were chosen so that the degree of dephasing of fat peaks matched between 3 T and 7 T.

The TE was chosen based on previous attempts of FAC quantification using 7 T, where a very short ΔTE proved crucial in bone marrow adipose tissue FAC quantification. (25)

Table 2: Table of acquisition parameters.

	First TE [ms]	ΔTE/2 [ms]	TR [ms]	Bandwidth [hz/pixel]	Pixel size [mm]	Slice Thickness [mm]	Number of Slices	Number of Echoes
3T	2.94	1.33	26	945	0.9x0.9	5	22	8
3T Interleaved	4.26	-	-	-	-	-	22	8
7T	1.26	0.57	30	1478	0.9x0.9	5	22	8
7T Interleaved	1.83	-	-	-	-	-	22	8

At 7 T, a first guess of the B0 map was obtained using the built-in mDixon Quant algorithm (Philips). At 3 T, a first guess of B0 was obtained using an off-line region-growing algorithm (28).

ROI Selection

When drawing the ROIs (Regions-of-Interest) in the phantoms, a simple bounding box was drawn using Python. The ROIs were drawn in an image of the signal intensity of the phantoms in grayscale, from parts of the phantoms where the signal intensity was as homogenous as possible. The same ROIs were used for all estimated variables.

Image Analysis

The acquired image data was evaluated using self-developed algorithms in python. SFA and PUFA were calculated for both 3 T and 7 T, and for all three reconstruction models. Both iterative steps used twelve echoes for the calculations.

Phantoms were evaluated by calculating means within the created ROIs of the phantoms. These means were compared to the theoretical FAC values of the phantoms and plotted as a scatterplot with linear regressions, Bland-Altman analysis of experimental values against theoretical values were also carried out.

Relative errors were also calculated. This was done by comparing one 80% phantom and one 100% phantom of the same butter type. Means were calculated using a different amount of data points (echoes), depending on the amount of data points needed for each model. The relative errors were calculated as %-deviation from theoretical value against number of data points. This would show how robust the

results are to changes and errors in the models. The relative error was calculated for phantom 1a and 1b.

Results

Early Phantom Trials

The following section shows the results from early attempts at creating a phantom setup and controlling T2* using temperature and sponges. Attempts to lower T2* either using temperature or sponges resulted in artifacts. The attempt to increase T2* in clarified butter by heating the phantoms before the measurement did not have the desired effect on T2*.

By changing the phantoms' temperature, and with this, making it liquid, or more solid, the value of T2* was expected to change. The wanted effect was that the warm 100% fat phantoms would have vastly longer T2* compared to the T2* of the 80% fat phantoms. However, as can be seen in figure 3, the change in T2* was not as large as expected, and the frozen 100% fat phantoms were closer to the warm 100% fat phantoms in T2*, than to the 80% fat phantoms. The expectation was to have a larger gap of T2* between each group of phantoms.

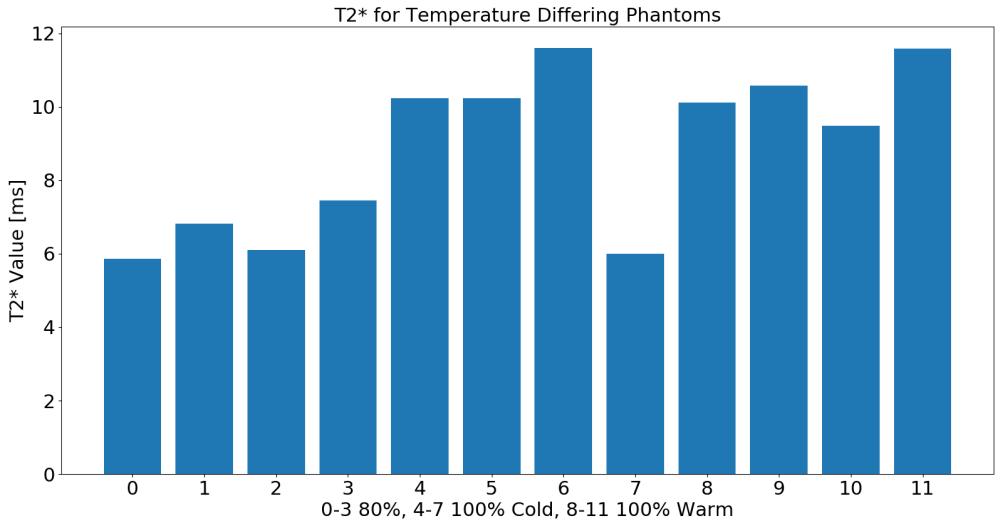

Figure 3: Values of T2* for each phantom. Phantoms correspond to the 80% and 100% cold and warm butter phantoms as shown in figure 4.

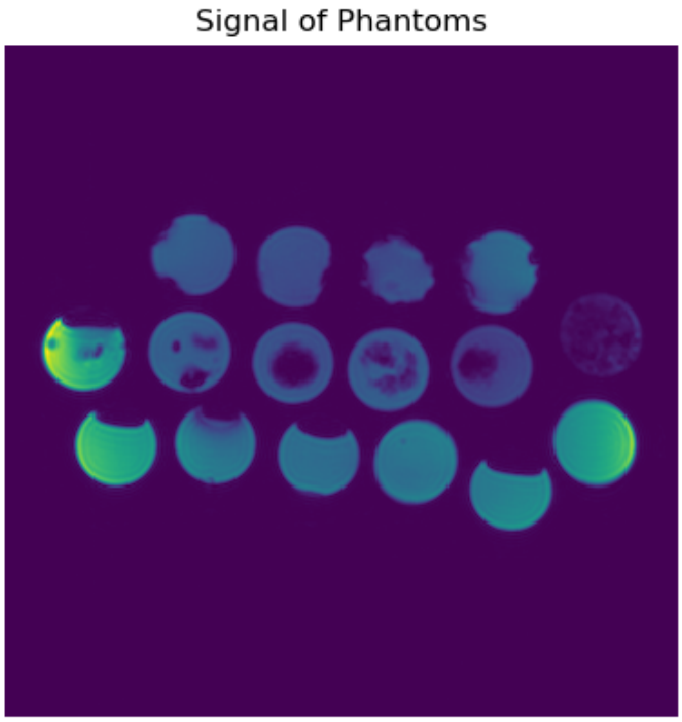

Figure 4: First row is 80% butter in room temperature, second row is from left to right: peanut butter oil, four butters, and coconut oil. The four butters in the middle row are frozen and ~100% PDFF. Last row is the same as the middle row, except they were warm before the measurement, meaning they were liquid. And as can be seen in the four phantoms in the middle row there are large areas of very low signal.

The phantom setup in figure 4 had a large temperature difference between phantoms in an attempt to emulate different T2*. This was done by having one set of the clarified butter as liquid, one set of clarified butter as frozen solid, and one set of room temperature 80% fat butter. This did not have the desired effect. The frozen phantoms had vast signal voids, likely due to extremely short T2*, which made evaluating them difficult.

The result of using sponges can be seen in figure 5, where areas with small dark spots as a result of air bubbles in the sponges can be seen in some phantoms. No further investigation of T2* was conducted in the phantoms in figure 5.

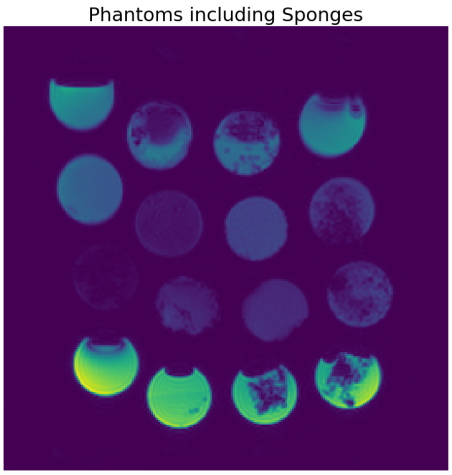

Figure 3: Early phantom setup that shows the result of using sponges in the oils in an attempt to simulate cancellous bone.

Final Phantom Trials

Butter and clarified butter in room temperature has proven to be a good alternative in creating an FAC-range with low T2* for different PDFF. A setup of long T2* phantoms could not be created, and thus the study is conducted only for short T2* FAC phantoms.

After several attempts and measurements, a final phantom setup was chosen. This setup consisted of six 80% fat phantoms, six 100% fat phantoms with identical FAC to the 80% fat phantoms, and four phantoms to measure different PDFF. The phantom setup can be seen in figure 2.

Figure 4: The signal of each phantom for 3T and 7T.

The pictures above (figure 6) show the signal of the last phantom trials, 3 T to the left, and for 7 T on the right.

The same signal-voids that can be seen in figure 4 can also be seen to some extent in some phantoms, albeit lesser, in figure 6, both for 3 T and 7 T.

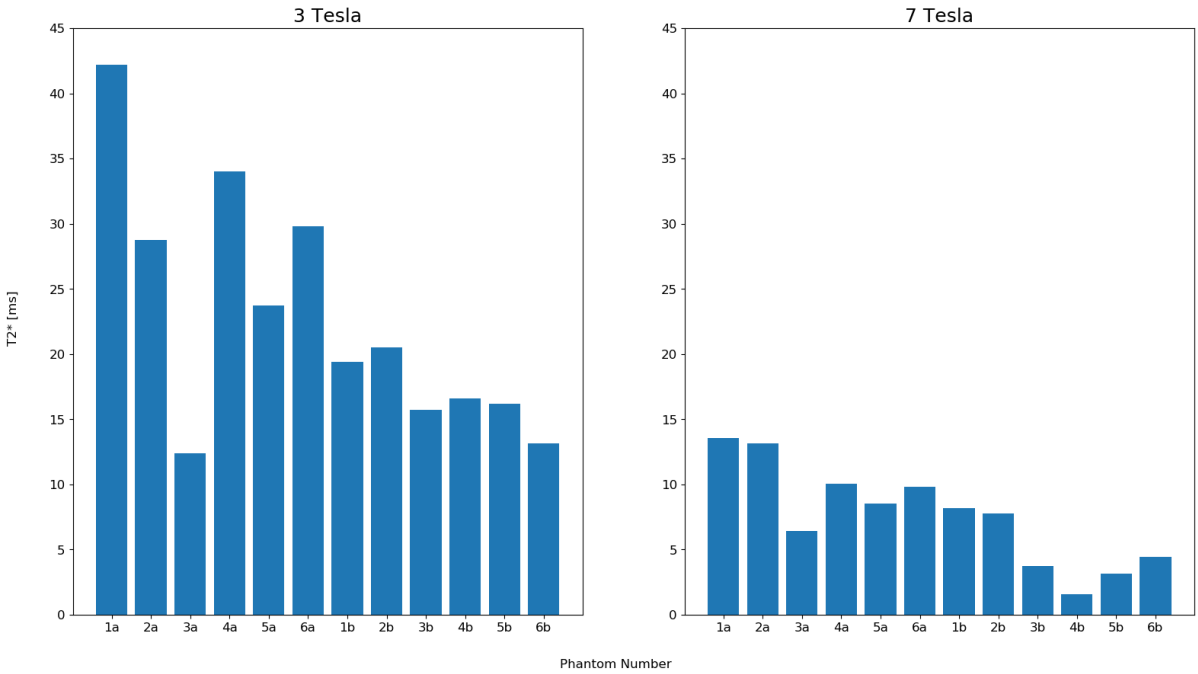

Figure 5: Estimated T2* for 3 T and 7 T for the final phantom setup as seen in figure 2.

In figure 7 above, the difference in T2* between the two systems is made quite clear. The 3 T system has almost three times as long T2* relaxation times compared to the 7 T system for most phantoms.

Comparisons

In this section, comparisons between the MRI systems and the three reconstruction models are presented. Quantitative parameter maps, scatterplots, relative errors and values for slope, intercept, average bias, and limits of agreement are shown for each parameter.

The scatterplots show the calculated experimental values compared with the theoretical values. Each plot also contains the linear regression (Slope and Intercept) of each fat fraction set (80% and 100%).

The relative error plots show the robustness of the different models for each field strength, for each variable. Each model has a different number of minimum datapoints (x-axis) for the calculations.

A perfect agreement would correspond to slope = 1, intercept = 0, average bias = 0 and narrow limits of agreement. A perfect robustness would result in the same, low relative error for all tested number of echoes.

PDFF

Overall, PDFF show high agreement and robust results. As can be seen in table 3, PDFF estimations agreed well with the theoretical values as slopes are close to one, small average bias and narrow limits of agreement.

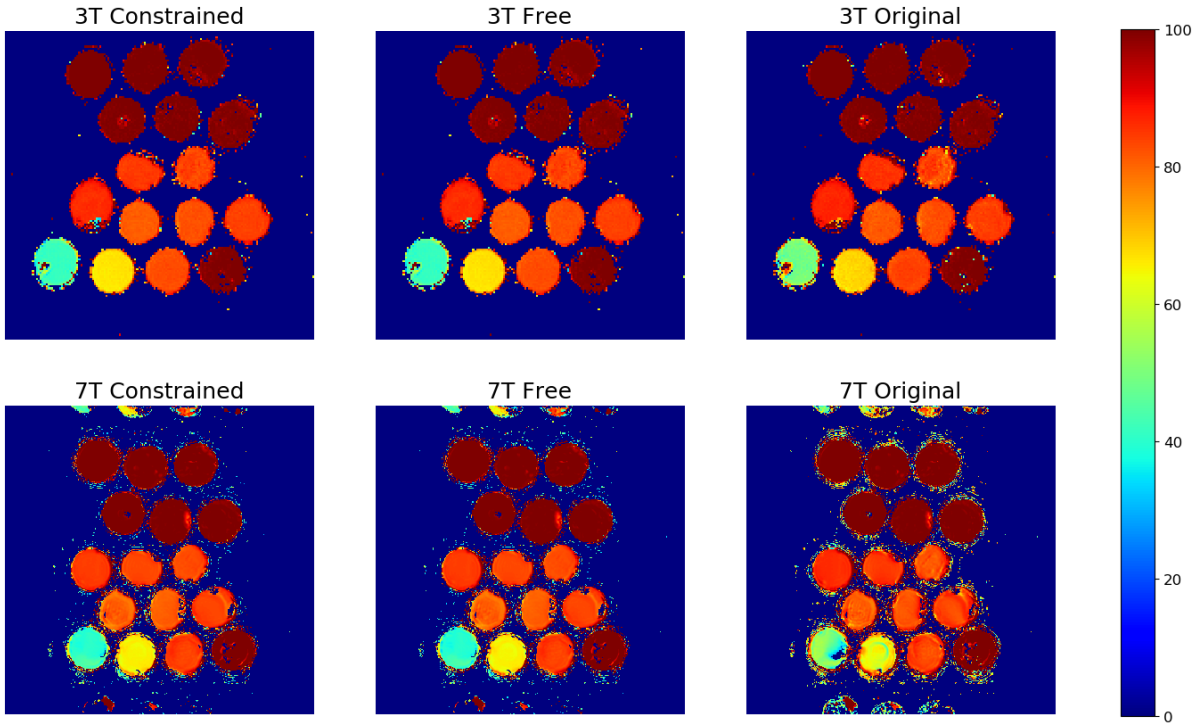

Figure 6: PDFF% of each phantom. The trend of PDFF in the phantoms is as expected and the phantoms are homogenous.

As can be seen in figure 8, the results for 7 T look slightly less homogeneous compared to the results for 3 T. But in general, the overall trend of PDFF in the phantoms is as expected.

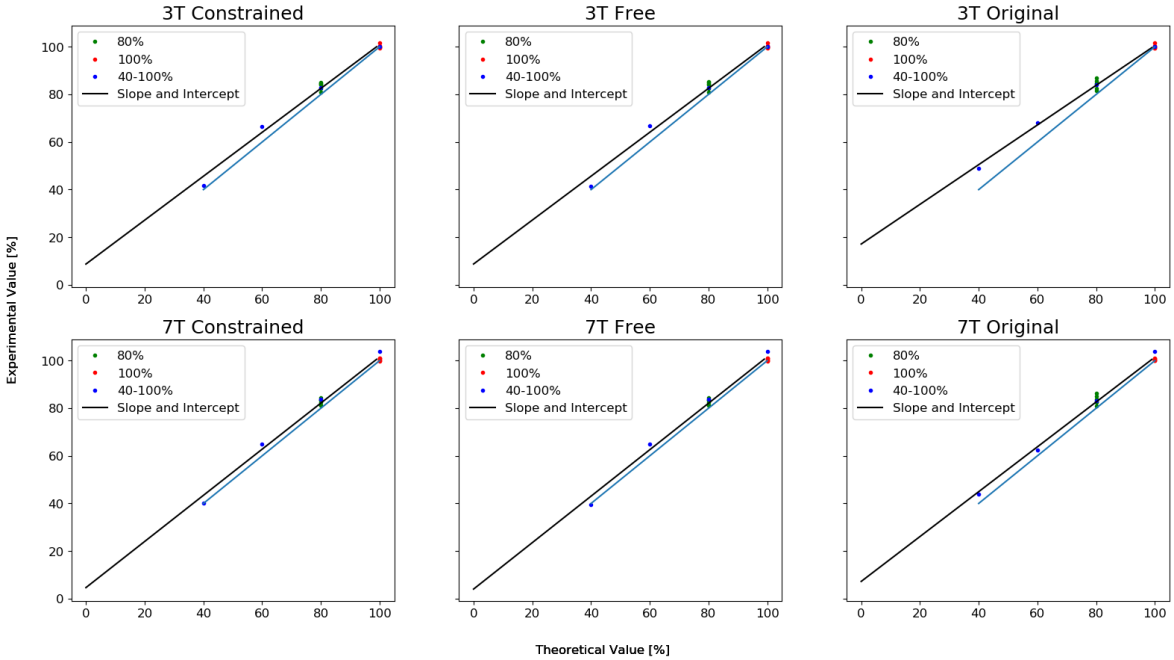

Figure 7: PDFF scatterplot for each model and both field strengths. Similar agreement can be seen over all models and both field strengths. Blue line represents the identity line.

Figure 9 shows how well the models estimate the total fat content of the phantoms. The blue identity line indicates an exact agreement to theoretical values. As can be

seen, the estimation of the 100% FAC phantoms is slightly more precise than that of the 80% FAC phantoms.

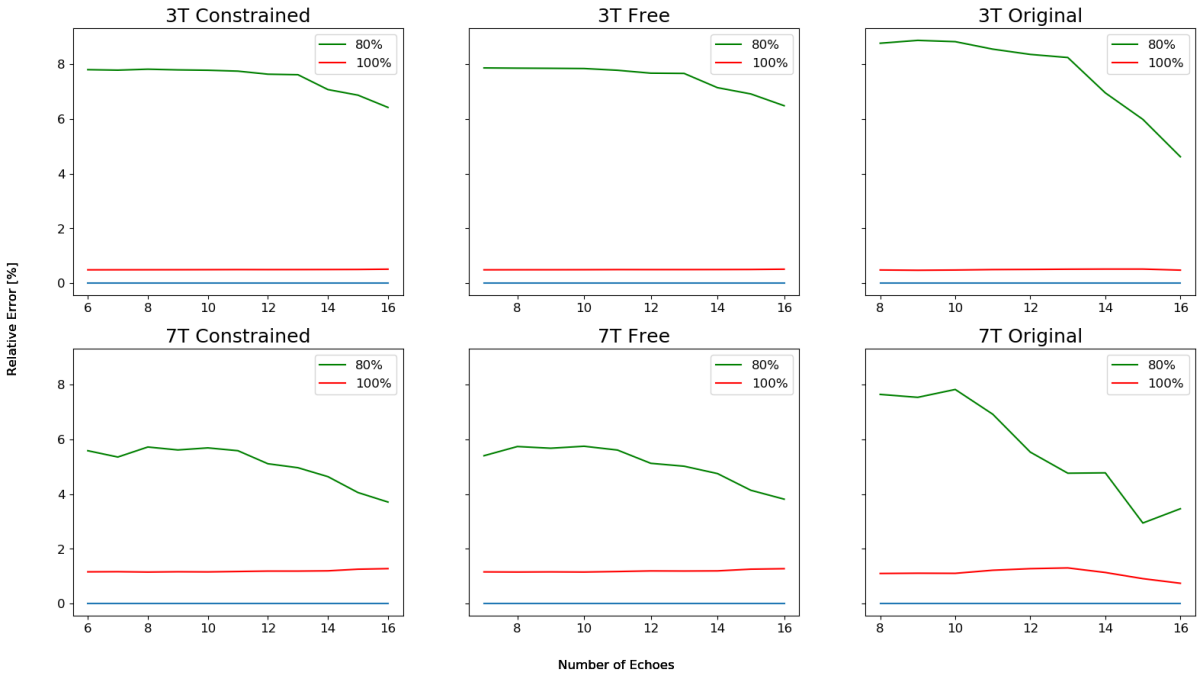

Figure 8: Relative error of Proton Density Fat Fraction shown in % deviation against number of datapoints used in the second calculation step. 3 T constrained and free model show the highest robustness.

The results for PDFF in figure 10 show that fewer echoes in the second calculation step gives more robust results and is less prone to variation in the results due to changes in the method. 3 T looks to be more robust than 7 T for PDFF. Here, the constrained and the free models are similar for 3 T.

Table 3: Slope, intercept, average bias, and agreement for PDFF from linear regression and Bland-Altman analysis.

	Slope	Intercept	Average Bias	Limits of Agreement
Constrained				
3T	0.92	8.73	-2.14	±4.25
7T	0.97	4.65	-2.01	±3.35
PDFF				
Free				
3T	0.92	8.75	-2.16	±4.39
7T	0.97	4.03	-1.97	±3.38
PDFF				
Original				
3T	0.83	17.15	-3.00	±5.99
7T	0.94	7.25	-2.34	±3.55

SFA

Overall, there was a tendency of underestimation with the SFA results, as can be seen by slopes < 1 and negative average bias (table 4).

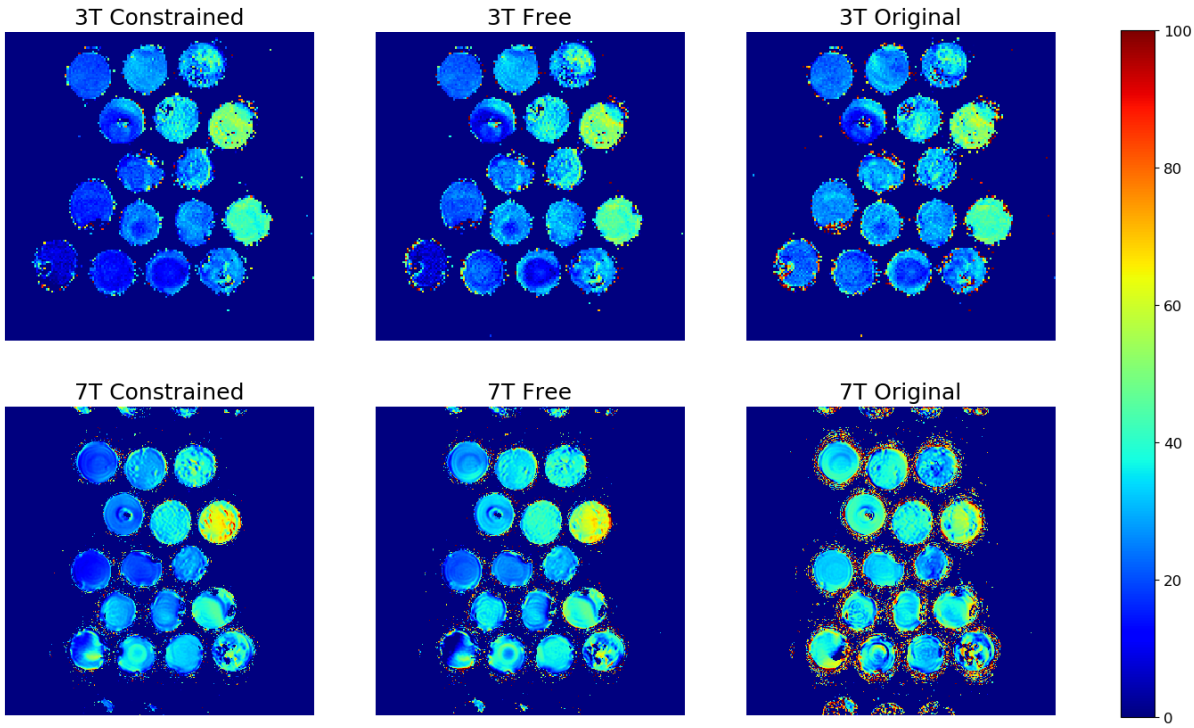

Figure 9: Figure containing SFA% for each phantom. The trend of increasing SFA from left to right in the first twelve phantoms is as expected.

As can be seen from the image above (figure 11), there are differences in the SFA estimation between 3 T and 7 T, and between the different models. Top twelve phantoms have increasing SFA from left to right. The 7 T results, especially for the original model, appear less homogenous than those for 3 T.

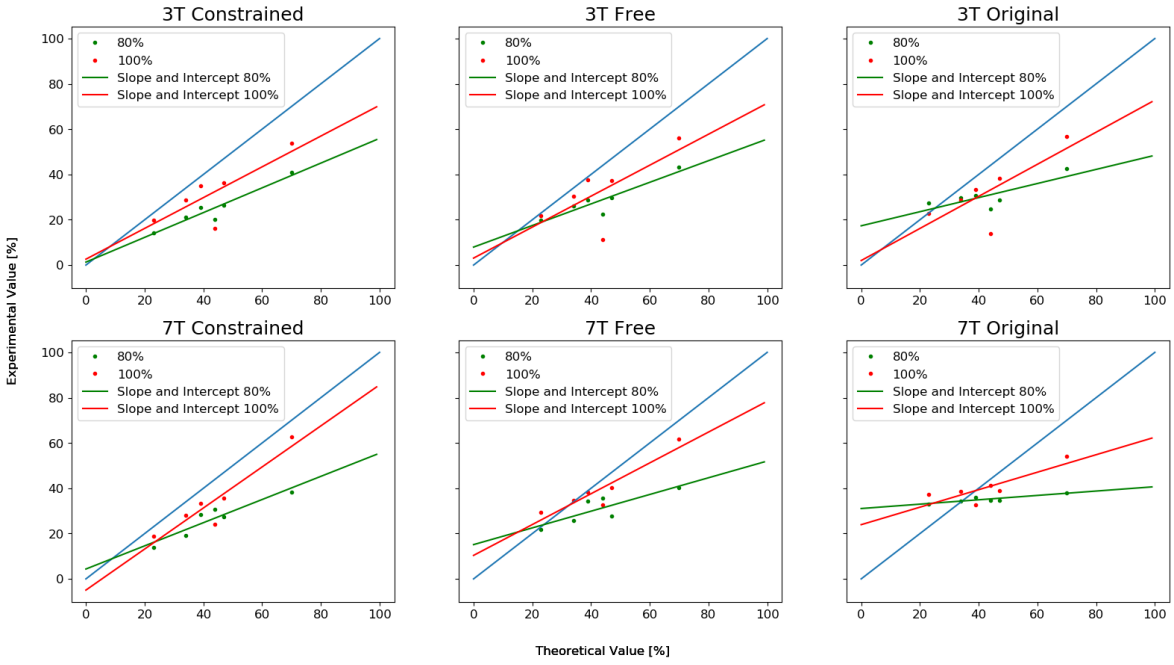

Figure 10: SFA scatterplot for each model and both field strengths. Less difference between 80- and 100% for 3 T. Constrained has better agreement than free and original.

Figure 12 above shows the estimations of SFA for each model and for 3 T and 7 T. As can be seen in the scatterplots, there is a trend of underestimation of SFA. The difference between values for 80- and 100% sets is smaller for 3 T than for 7 T. Constrained and free model estimates of SFA, looking at the linear regression, show higher agreement than the estimates from original model. 3 T constrained model looks superior in estimating SFA compared to the other models.

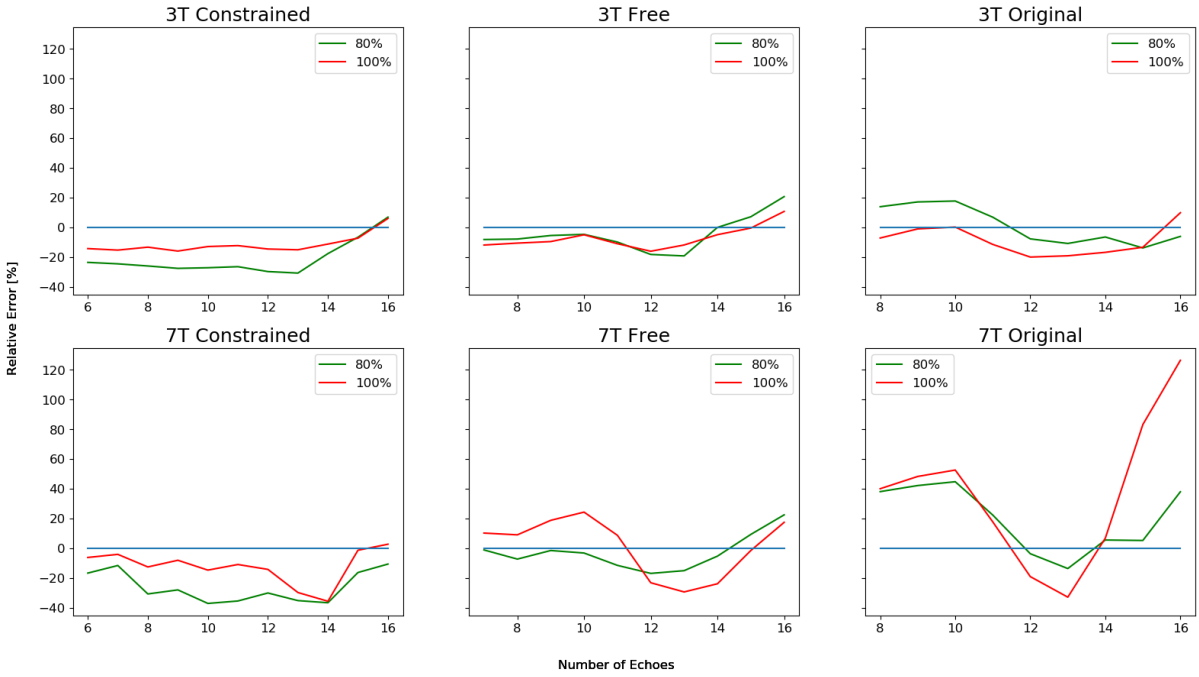

Figure 11: Relative error of SFA shown as % deviation against number of datapoints used in calculation. Constrained 3 T model shows the most robustness compared to the other models and 7 T.

Similar to the results for PDFF, generally, fewer echoes give more robust results for SFA (figure 13). Constrained model shows more robustness than free and original, and 3 T is more robust than 7 T.

Table 4: Slope, intercept, average bias, and agreement for SFA from linear regression and Bland-Altman analysis.

	Slope	Intercept	Average Bias	Limits of Agreement
Constrained				
3T				
80%	0.54	1.31	-18.12	±13.75
100%	0.68	2.60	-11.13	±17.05
7T				
80%	0.51	4.36	-16.57	±14.91
100%	0.90	-4.94	-8.97	±10.56
Free				
3T				
80%	0.48	7.93	-14.48	±15.93
100%	0.68	3.08	-10.47	±21.52
7T				
80%	0.37	15.13	-11.90	±19.09
100%	0.68	10.38	-3.31	±11.86
Original				
3T				
80%	0.31	17.33	-12.17	±20.65
100%	0.70	2.010	-10.50	±18.85
7T				
80%	0.10	31.06	-7.64	±25.52
100%	0.38	23.94	-2.36	±18.76

PUFA

In general, an overestimation of PUFA was obtained. This can be seen by slopes > 1 and mainly positive average bias (table 5).

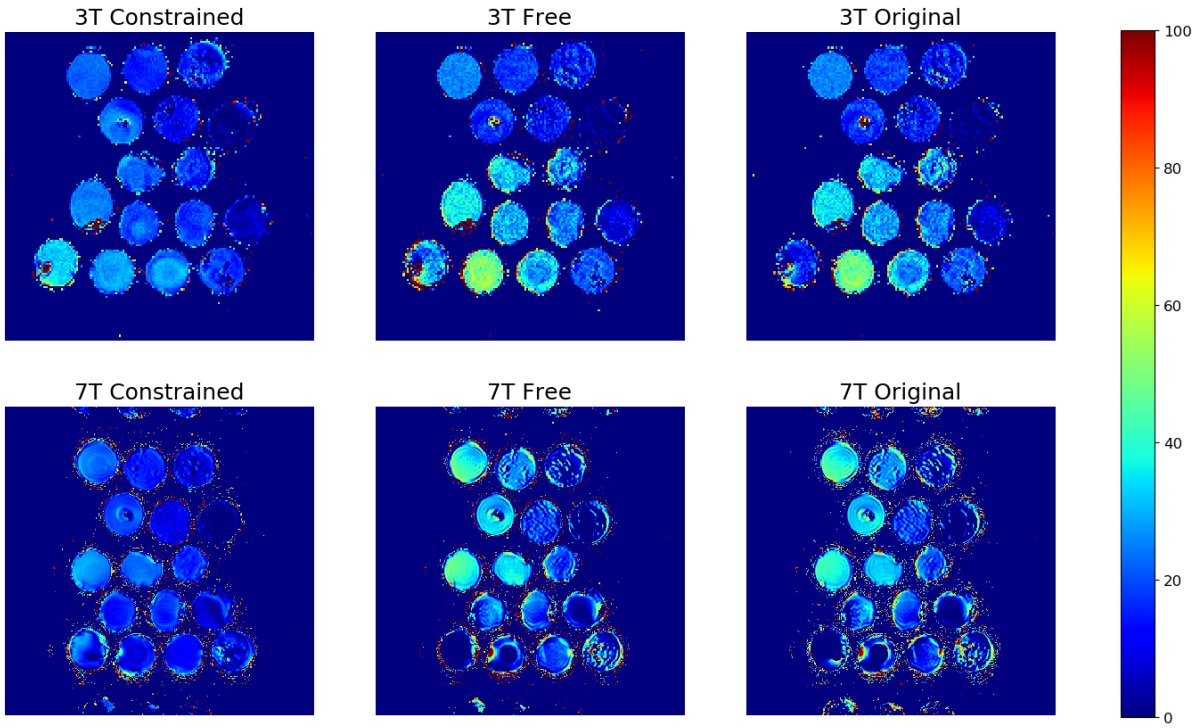

Figure 12: PUFA% of each phantom. The trend of decreasing PUFA from left to right in the first twelve phantoms is as expected.

With this phantom setup, PUFA decreases from left to right on the top twelve phantoms, as can be seen in figure 14. PUFA is, however, not as homogenous as SFA. Just as for SFA, the 7 T results appear less homogenous than the 3 T results, especially for the original model. Phantom 6a is as dark as it is because the value has been estimated as negative.

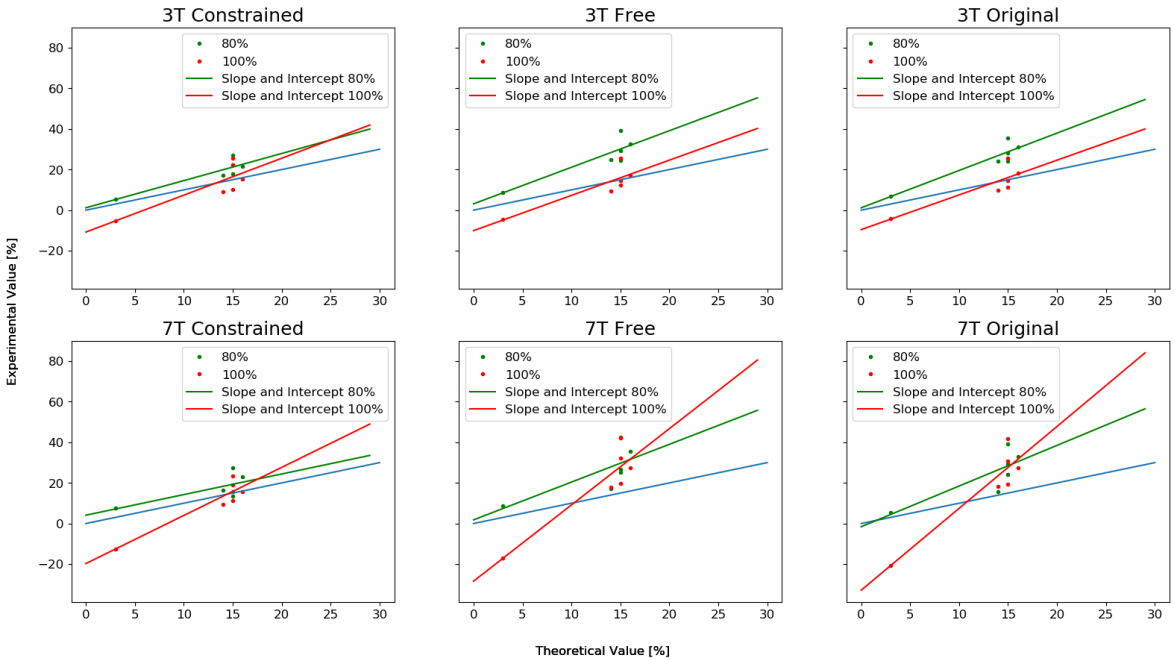

Figure 13: PUFA scatterplot for each model, and for both field strengths. Better agreement for 3 T compared to 7T. Constrained has better agreement than free and original models. Less variation for constrained model between 80- and 100%.

As can be seen in figure 15 above, 3 T constrained model resulted in a better agreement to the theoretical values compared to the free and original models, and 7 T. However, due to the small variation of the theoretical values, the linear regression is hard to interpret.

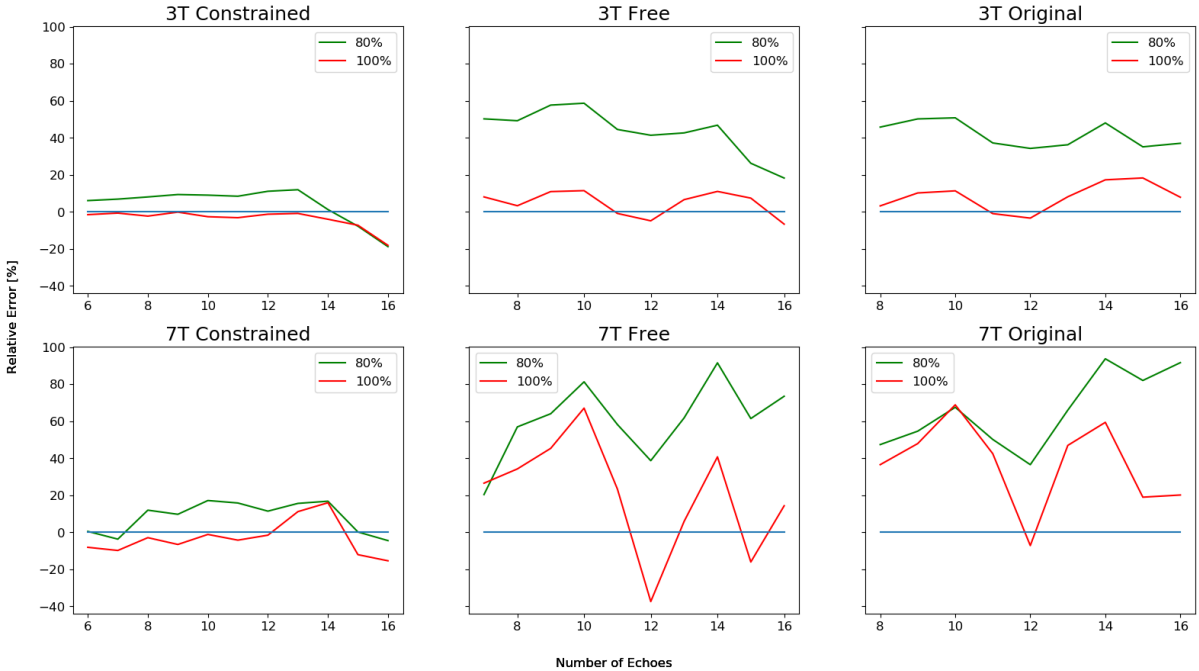

Figure 14: Relative error of PUFA shown as % deviation against number of datapoints used in the calculations. Here, the 3 T constrained shows the highest robustness.

The relative error for PUFA (figure 16) shows the same trend as for SFA and PDFF. Constrained models show higher robustness compared to free and original, and 3 T is more robust than 7 T.

Table 5: Slope, intercept, average bias, and agreement for PUFA from linear regression and Bland-Altman analysis.

	Slope	Intercept	Average Bias	Limits of Agreement
Constrained				
3T				
80%	1.33	1.18	5.57	±6.72
100%	1.81	-10.78	-0.15	±13.41
7T				
80%	1.01	4.10	4.3	±8.96
100%	2.36	-19.72	-1.92	±14.67
Free				
3T				
80%	1.80	3.10	13.53	±11.50
100%	1.73	-10.08	-0.52	±11.28
7T				
80%	1.86	1.79	12.99	±16.32
100%	3.75	-28.41	7.42	±28.47
Original				
3T				
80%	1.84	1.15	12.08	±10.24
100%	1.71	-9.58	-0.35	±11.28
7T				
80%	2.00	-1.57	11.47	±15.64
100%	4.03	-32.86	6.57	±30.44

Discussion

The aims of this study were to optimize a method and develop an algorithm that can be used to quantify FAC in bone marrow adipose tissue. Also, to compare reconstruction models and field strengths of 3 T and 7 T. Lastly, to develop a reference phantom with bone marrow-like characteristics.

Overall, using fewer echoes in the second calculation step seems to be more robust and less prone to error due to changes in the model. The 3 T estimations appear to be in closer agreement to the theoretical values compared to the estimated values at 7 T. 3 T also show less difference in the estimation of FAC due to changes in PDFF compared to 7 T. Commercial butters seem to be a good alternative for phantoms to achieve an FAC-range with low T2*. The self-developed python algorithm enables FAC quantification from images acquired at 3 T and 7 T and using both Siemens and Philips scanners. However, the phantoms may need some extra work to also enable measurements for long T2* and identical FAC.

Our measured results did not match the theoretical results perfectly, there are several possible sources of error that may have affected the results. There might be a slight error source in creating the clarified butter phantoms, as there might not have been a perfect separation of the water and oil phase. However, remaining proteins are expected to sink to the bottom of the phantom vial leaving most of the phantom vial unaffected.

Further, the final measurements were done in room temperature; however, the fat/water shift is temperature dependent, and the used fat frequency model is based on in vivo measurements in body temperature. Warming the butter to body temperature may affect its composition, which would most likely create even more errors in the measurements. Also, managing to keep the same temperature of the butter during the measurement would have been hard to achieve. The effect of temperature on fat quantification has been found to be a confounding factor (29), this makes doing fat quantification in phantoms potentially harder than fat quantification in vivo.

Assumptions of nmidb and cl are based on measurements in subcutaneous fat (22), however, there might be a different relationship for butter. This can affect the results of the calculations of parameters connected to nmidb and cl.

There was an attempt to make the sequences between 3T and 7T as similar as possible, however, creating two sequences that have the exact same parameters between systems is not easy. This means that some source of error might occur between the systems for 3T and 7T, since the 3T is a Siemens Prisma system, and the 7T is a Philips Achieva system.

Another source of error that might affect the imaging sequence used, are eddy currents, which have not been accounted for. Eddy currents create a magnetic field that oppose the pulsed magnetic fields, which will create a phase distortion of the encoding of magnetic spins. The eddy currents decay exponentially, and therefore affect the first echoes the most (30). Eddy currents can negatively affect fat-water separation, mainly in the readout direction (31, 32).

PUFA seem to be the most sensitive variable in the estimation, as it and nmidb is usually far from the theoretical values. PUFA and nmidb are for some reason a lot more prone to error in the calculation. More work would be needed to find out why PUFA seems to be more sensitive than SFA. More PUFA measurements need to be done with a wider range of PUFA.

There could be a slight impact on the results within each phantom because of T1 and T2 bias between the different fat peaks, and between fat and water (33).

Some of the frozen phantoms had large signal voids, as can be seen in figure 4. The signal voids appear to be related to areas of extremely short T2*, but the reason is unclear. Potentially, a difference in freezing point depending on fatty acid composition may help explain why only some phantoms vials were affected.

In this work, FAC was estimated in a two-step process, where fat, water, the complex field map, and the complex errors were estimated in a first step followed by a second iteration estimating the fatty acid composition parameters. A one-step iteration was also tested, simultaneously estimating all parameters, however, a two-

step process resulted in more robust results and was chosen for the remainder of the work (data not shown).

This study had some limitations, for example, comparing the methods with short and long T2* in phantoms could not be done, as phantoms with identical FAC but vastly different T2*-relaxation times could not be constructed.

In this work, only FAC in phantoms were estimated. Further studies using the proposed method for in vivo FAC estimation in bone marrow adipose tissue, as well as validation against GC, are needed.

Conclusion

Commercial butters are reasonable reference phantoms to simulate tissue with short T2* for a range of FAC values. The self-developed Python algorithm is able to quantify FAC for both 3 T and 7 T. For future studies of FAC in bone marrow adipose tissue, 3 T would be preferred over 7 T. A constrained approach would be preferred over the free or original model.

Acknowledgements

Thanks to Pernilla Peterson for pristine supervising and Andrea Fingerhut for assisting with all questions Python and troubleshooting.

References

1. Hamilton G, Yokoo T, Bydder M, Cruite I, Schroeder ME, Sirlin CB, et al. In vivo characterization of the liver fat (1)H MR spectrum. NMR Biomed. 2011;24(7):784-90.
2. Peterson P, Mansson S. Simultaneous quantification of fat content and fatty acid composition using MR imaging. Magn Reson Med. 2013;69(3):688-97.
3. Martel D, Leporq B, Bruno M, Regatte RR, Honig S, Chang G. Chemical shift-encoded MRI for assessment of bone marrow adipose tissue fat composition: Pilot study in premenopausal versus postmenopausal women. Magn Reson Imaging. 2018;53:148-55.
4. Martel D, Leporq B, Saxena A, Belmont HM, Turyan G, Honig S, et al. 3T chemical shift-encoded MRI: Detection of altered proximal femur marrow adipose tissue composition in glucocorticoid users and validation with magnetic resonance spectroscopy. J Magn Reson Imaging. 2019;50(2):490-6.
5. Lippiello L, Walsh T, Fienhold M. The association of lipid abnormalities with tissue pathology in human osteoarthritic articular cartilage. Metabolism. 1991;40(6):571-6.
6. Plumb MS, Aspden RM. High levels of fat and (n-6) fatty acids in cancellous bone in osteoarthritis. Lipids Health Dis. 2004;3:12.
7. Loeser RF, Goldring SR, Scanzello CR, Goldring MB. Osteoarthritis: a disease of the joint as an organ. Arthritis Rheum. 2012;64(6):1697-707.
8. Barnett R. Osteoarthritis. Lancet. 2018;391(10134):1985.
9. Englund M. AT. Artros allt vanligare folksjukdom. Läkartidningen 2014,111:CSDU. 2014.
10. Eckstein F, Kwoh CK, Link TM, investigators OAI. Imaging research results from the osteoarthritis initiative (OAI): a review and lessons learned 10 years after start of enrolment. Ann Rheum Dis. 2014;73(7):1289-300.
11. Felson DT, Lawrence RC, Hochberg MC, McAlindon T, Dieppe PA, Minor MA, et al. Osteoarthritis: new insights. Part 2: treatment approaches. Ann Intern Med. 2000;133(9):726-37.
12. Travlos GS. Normal structure, function, and histology of the bone marrow. Toxicol Pathol. 2006;34(5):548-65.

13. Hartsock RJ, Smith EB, Petty CS. Normal Variations with Aging of the Amount of Hematopoietic Tissue in Bone Marrow from the Anterior Iliac Crest. A Study Made from 177 Cases of Sudden Death Examined by Necropsy. Am J Clin Pathol. 1965;43:326-31.
14. Ricci C, Cova M, Kang YS, Yang A, Rahmouni A, Scott WW, Jr., et al. Normal age-related patterns of cellular and fatty bone marrow distribution in the axial skeleton: MR imaging study. Radiology. 1990;177(1):83-8.
15. Verma S, Rajaratnam JH, Denton J, Hoyland JA, Byers RJ. Adipocytic proportion of bone marrow is inversely related to bone formation in osteoporosis. J Clin Pathol. 2002;55(9):693-8.
16. Wang L, Salibi N, Chang G, Vieira RL, Babb JS, Krasnokutsky S, et al. Assessment of subchondral bone marrow lipids in healthy controls and mild osteoarthritis patients at 3T. NMR Biomed. 2012;25(4):545-55.
17. Wang L, Salibi N, Chang G, Bencardino JT, Babb JS, Rokito A, et al. Evaluation of subchondral bone marrow lipids of acute anterior cruciate ligament (ACL)-injured patients at 3 T. Acad Radiol. 2014;21(6):758-66.
18. Tufts LS, Shet K, Liang F, Majumdar S, Li X. Quantification of bone marrow water and lipid composition in anterior cruciate ligament-injured and osteoarthritic knees using three-dimensional magnetic resonance spectroscopic imaging. Magn Reson Imaging. 2016;34(5):632-7.
19. Li X, Ma BC, Bolbos RI, Stahl R, Lozano J, Zuo J, et al. Quantitative assessment of bone marrow edema-like lesion and overlying cartilage in knees with osteoarthritis and anterior cruciate ligament tear using MR imaging and spectroscopic imaging at 3 Tesla. J Magn Reson Imaging. 2008;28(2):453-61.
20. Ren J, Dimitrov I, Sherry AD, Malloy CR. Composition of adipose tissue and marrow fat in humans by 1H NMR at 7 Tesla. J Lipid Res. 2008;49(9):2055-62.
21. Hodson L, Skeaff CM, Fielding BA. Fatty acid composition of adipose tissue and blood in humans and its use as a biomarker of dietary intake. Prog Lipid Res. 2008;47(5):348-80.
22. Trinh L, Peterson P, Leander P, Brorson H, Mansson S. In vivo comparison of MRI-based and MRS-based quantification of adipose tissue fatty acid composition against gas chromatography. Magn Reson Med. 2020;84(5):2484-94.
23. Pohmann R, Speck O, Scheffler K. Signal-to-noise ratio and MR tissue parameters in human brain imaging at 3, 7, and 9.4 tesla using current receive coil arrays. Magn Reson Med. 2016;75(2):801-9.
24. Juchem C, de Graaf RA. B0 magnetic field homogeneity and shimming for in vivo magnetic resonance spectroscopy. Anal Biochem. 2017;529:17-29.
25. SEVGI EMIN JS, MARTIN ENGLUND, PERNILLA PETERSON. Fatty acid composition quantification in bone marrow at 7 T:

method comparison and in vivo feasibility. In: Universitet L, editor. 2021.
26. Peterson P, Mansson S. Fat quantification using multiecho sequences with bipolar gradients: investigation of accuracy and noise performance. Magn Reson Med. 2014;71(1):219-29.
27. Soliman AS, Wiens CN, Wade TP, McKenzie CA. Fat quantification using an interleaved bipolar acquisition. Magn Reson Med. 2016;75(5):2000-8.
28. Berglund J, Johansson L, Ahlstrom H, Kullberg J. Three-point Dixon method enables whole-body water and fat imaging of obese subjects. Magn Reson Med. 2010;63(6):1659-68.
29. Hernando D, Sharma SD, Kramer H, Reeder SB. On the confounding effect of temperature on chemical shift-encoded fat quantification. Magn Reson Med. 2014;72(2):464-70.
30. J. J. VAN VAALST AHB. Optimization of Eddy-Current Compensatio. JOURNAL OF MAGNETIC RESONANCE. 1990(90):52-70.
31. Hernando D, Hines CD, Yu H, Reeder SB. Addressing phase errors in fat-water imaging using a mixed magnitude/complex fitting method. Magn Reson Med. 2012;67(3):638-44.
32. Yu H, Shimakawa A, Hines CD, McKenzie CA, Hamilton G, Sirlin CB, et al. Combination of complex-based and magnitude-based multiecho water-fat separation for accurate quantification of fat-fraction. Magn Reson Med. 2011;66(1):199-206.

33. Peterson P, Svensson J, Mansson S. Relaxation effects in MRI-based quantification of fat content and fatty acid composition. Magn Reson Med. 2014;72(5):1320-9.